

Proceeding Paper

Analysis of Multipath Code-Range Errors in Future LEO-PNT Systems [†]

Sibren De Bast ^{1,2,*} , Jean-Marie Sleewaegen ¹  and Wim De Wilde ¹ 

¹ Septentrio NV, 3001 Leuven, Belgium

² Networked Systems, Department of Electrical Engineering (ESAT), KU Leuven, 3001 Leuven, Belgium

* Correspondence: sibren.debast@septentrio.com

[†] Presented at the European Navigation Conference 2023, Noordwijk, The Netherlands, 31 May–2 June 2023.

Abstract: In recent years, low-Earth-orbit (LEO) constellations have been proposed for Positioning, Navigation and Timing (PNT) applications. Moreover, a couple of test satellites have already been launched and many more are scheduled in the near future. LEO constellations are characterised by their rapid change in geometry in comparison to the current medium-Earth-orbit (MEO) Global Navigation Satellite Systems (GNSSs). In this study, we analyse the impact of this high geometry change rate on the code-range error induced by multipaths. We develop a simulation environment with a static receiver and a nearby large building. We track the multipath signal using classical delay- and phase-locked loops (DLL and PLL). Multiple scenarios are simulated and analysed, comparing different orbit heights, MEO and LEO, and carrier frequencies (L-, S- and C-band). The LEO scenarios show up to 96% less code-range error for fast-changing multipath components. We show that this phenomenon is linked to the large phase delay rate between the direct signal and the multipath components, which is up to 75 times higher for LEO satellites when compared to MEO satellites. The phase delay rate reaches values higher than the DLL bandwidth. As a result, the DLL filters out the errors induced by fast-changing reflected signals, partially eliminating the multipath-induced code-range errors. The presented effect is coupled to the wavelength of the used carrier frequency. Our simulations show a reduction in multipath-induced code-range error for S- and C-band LEO-PNT signals in comparison to L-band signals.

Keywords: GNSS; multipath; LEO; PNT



Citation: De Bast, S.; Sleewaegen, J.-M.; De Wilde, W. Analysis of Multipath Code-Range Errors in Future LEO-PNT Systems. *Eng. Proc.* **2023**, *54*, 34. <https://doi.org/10.3390/ENC2023-15453>

Academic Editors: Tom Willems and Okko Bleeker

Published: 29 October 2023



Copyright: © 2023 by the authors. Licensee MDPI, Basel, Switzerland. This article is an open access article distributed under the terms and conditions of the Creative Commons Attribution (CC BY) license (<https://creativecommons.org/licenses/by/4.0/>).

1. Introduction

Global Navigation Satellite Systems (GNSSs) are a cornerstone of modern life. They provide location and timing services that play a crucial role in the localisation of several-billion GNSS-enabled mobile devices. Moreover, they are used to regulate and synchronise critical infrastructure such as telecommunication networks and power grid infrastructure. Current GNSS systems are MEO constellations, consisting of tens of satellites. They can provide meter-level accuracy in stand-alone mode or centimetre-level when using advanced algorithms and augmentation signals.

Interest in LEO-PNT systems has skyrocketed in recent years. LEO-based systems promise a couple of benefits, for example, higher resilience to jamming due to a higher received power and a faster convergence time for Precise Point Positioning (PPP) [1].

In addition, the global space economy has changed recently, lowering the cost of launching satellites to low-Earth orbit. This has given rise to the deployment of several telecommunication LEO mega-constellations. Moreover, several LEO constellations have been proposed specifically for PNT services. Several commercial companies have launched initial test satellites, for example, the PULSAR system from Xona Space Systems [2], the GeeSAT satellites from GeeSpace and the CentiSpace satellites from Future Navigation [3]. Governmental institutes are also interested, as the European Space Agency

(ESA) is planning to launch several LEO-PNT test satellites in the near future as part of the FutureNAV program.

The recent literature on LEO-PNT often mentions a decrease in multipath errors when using LEO in comparison to MEO satellites. Lawrence et al. [4] argue that when using LEO satellites, the multipath will whiten. In other words, the rapidly changing geometry of the LEO satellites makes the phase offset of the reflected signals resemble white noise and will be treated as that by the receiver. As a result, the induced multipath error will decrease.

Iannucci et al. [5] also mention that the rapidly changing geometry of LEO satellites will “average out” the multipath error. The paper gives a rough estimate of a 100 times larger geometry change in comparison to MEO counterparts. However, the exact value of this factor depends on the orbit height of the LEO satellite as this dictates the geometry change rate. In addition, they argue that the shorter wavelength of the used signals in LEO satellites will further increase the multipath decorrelation effect. The shorter wavelength increases the sensitivity of the relative phases of the multipath components to path-length differences. However, the authors focus on using broadband LEO satellites, which often operate at much higher frequencies than traditional GNSS satellites. The real impact of this effect will be determined by the used frequency of the LEO-PNT system.

Until now, the literature only provides back-of-the-envelope calculations. This work tries to overcome this by performing an analysis of the experienced multipath errors. A simulated LEO-PNT multipath environment is presented, using realistic signal values and material properties to study the multipath code-range errors in more depth.

This paper is organised as follows: Section 2 describes the system model. In Section 3, the simulation scenario is introduced. Afterwards, the results are discussed in Section 4. Section 5 concludes this study.

2. System Model

In this paper, we study a PNT signal affected by multipath propagation. The signal at the receiver is composed of $K + 1$ signal components and noise. The first component is the direct signal. This signal can freely propagate from the transmitting satellite to the receiver without encountering objects. The other K components are Non-Line-of-Sight (NLoS) components. These signals arrive delayed at the receiver through reflections. The resulting received signal is presented as follows:

$$s_{rx}(t) = \left(\sum_{k=0}^K A_k s(t - \Delta t_k) e^{j2\pi f_c(t - \Delta t_k) + \phi_k} \right) + n(t) \quad (1)$$

A_k is the amplitude of the signal component, $s(t)$ is the time-variant baseband signal, Δt_k is the time delay in comparison to the direct component, f_c is the carrier frequency and $n(t)$ is the noise. ϕ_k is the phase offset.

The amplitude A_k of each component relies on three factors: the Received Isotropic Power (RIP), the receiver antenna gain, and the polarisation change and attenuation induced by each reflection.

2.1. Received Isotropic Power (RIP)

The RIP dictates how much power is received when using an isotropic receiving antenna. The RIP is defined by the transmit power of the satellite, its antenna gain pattern and the distance between the satellite and the receiver. The RIP depends on the boresight angle of the receiver as seen from the satellite’s antenna; hence, on the receiving side, the RIP is dependent on the elevation angle θ_{el} of the satellite.

2.2. Receiver Antenna Gain Pattern

The gain pattern of the receiving antenna will boost or decrease the signal amplitude, depending on the direction of the incoming wave and its polarisation. A good GNSS antenna focuses on signals coming from a direction with a positive elevation angle while rejecting signals coming from the ground. In this way, ground reflections are partially miti-

gated. In addition, the antenna gain is dependent on the polarisation of the incoming wave. A receiving GNSS antenna has different gain characteristics for Right-Hand Circularly Polarised (RHCP) waves and Left-Hand Circularly Polarised (LHCP) waves. The signals transmitted by GNSS satellites are RHCP waves; therefore, GNSS antennas are optimised to boost RHCP waves and mitigate LHCP waves as these are the result of reflected signals.

2.3. Reflections and Signal Polarisation

The electric field of circularly polarised waves is constantly rotating in the direction perpendicular to the propagation direction of the wave. The rotation direction decides if it is right-handed- or left-handed-polarised.

The normalised electrical field of an RHCP wave is presented as a Jones vector as follows: [6]

$$E = \frac{1}{\sqrt{2}} \begin{bmatrix} 1 \\ -j \end{bmatrix} \quad (2)$$

The amplitude and polarisation of the wave change due to reflections, depending on the material properties of the reflection interface and the incidence angle of the incoming wave. A part of the incoming power is reflected back, while the rest is transmitted through the material. Reflections can be described by means of reflection coefficients, which represent how much of the power is reflected. A set of two reflection coefficients must be calculated, r_p and r_s . r_p corresponds to waves with an electric field in the plane of incidence and r_s to waves with an electric field normal to the plane of incidence. They can be calculated using the Fresnel equations. We note the m -th reflection in Jones vector notation as follows:

$$R_m = \begin{bmatrix} -r_{p,m} & 0 \\ 0 & r_{s,m} \end{bmatrix} \quad (3)$$

with

$$r_{p,m} = \frac{n_{1,m} \sqrt{1 - \left(\frac{n_{1,m}}{n_{2,m}} \sin \theta_{i,m}\right)^2} - n_{2,m} \cos \theta_{i,m}}{n_{1,m} \sqrt{1 - \left(\frac{n_{1,m}}{n_{2,m}} \sin \theta_{i,m}\right)^2} + n_{2,m} \cos \theta_{i,m}}, \quad (4)$$

$$r_{s,m} = \frac{n_{1,m} \cos \theta_{i,m} - n_{2,m} \sqrt{1 - \left(\frac{n_{1,m}}{n_{2,m}} \sin \theta_{i,m}\right)^2}}{n_{1,m} \cos \theta_{i,m} + n_{2,m} \sqrt{1 - \left(\frac{n_{1,m}}{n_{2,m}} \sin \theta_{i,m}\right)^2}}. \quad (5)$$

$\theta_{i,m}$ is the incidence angle of reflection m ; this is the angle between the direction of the incoming wave and the normal on the reflective surface. $n_{1,m}$ and $n_{2,m}$ are the refractive indices of the two materials. $n_{1,m}$ relates to the medium in which the incoming wave is propagating, while $n_{2,m}$ relates to the material on which the wave reflects.

The resulting reflection coefficient R after M reflections is calculated as follows:

$$R = \prod_{m=1}^M R_m \quad (6)$$

The reflected electric field is calculated by multiplying E and R of Equations (2) and (6). To calculate the impact of receiving reflected waves using a circularly polarised antenna, the reflection coefficient can be decomposed into an RHCP and an LHCP component [7]:

$$R_R = \frac{r_s + r_p}{2}, \quad R_L = \frac{r_s - r_p}{2} \quad (7)$$

Each component has to be multiplied by the respective antenna gain pattern of the receiving antenna. In general, the amplitude of a multipath signal component can be written as follows:

$$A_k = \sqrt{\text{RIP}(\theta_{el})} \sqrt{\left(\frac{R_R}{\sqrt{2}} G_{rx,R}(\theta_{rx})\right)^2 + \left(\frac{R_L}{\sqrt{2}} G_{rx,L}(\theta_{rx})\right)^2} \quad (8)$$

The RIP is a function of the elevation angle of the satellite θ_{el} . R is the reflection coefficient of the electric field of the signal, while the subscript $\{R, L\}$ denotes the polarisation of the component, RHCP and LHCP, respectively. The receiver antenna gain G_{rx} is dependent on the polarisation and on the angle of incidence of the signal θ_{rx} .

2.4. Signal Tracking

To estimate the code-ranging error, the signal has to be acquired and tracked. As the acquisition does not influence the multipath error, we assume a perfect acquisition at the start of tracking the signal. The signal tracking is performed using a classical delay-locked loop and phase-locked loop (DLL and PLL). Each of the loops has been tuned for MEO GNSS systems and is used without modification to track the LEO signals. Unless otherwise specified in Section 4, all results presented in this paper are generated using the following bandwidth (BW) values for the locked loops: $\text{BW}_{\text{DLL}} = 0.25$ Hz; $\text{BW}_{\text{PLL}} = 15$ Hz.

2.5. Limitations of the Model

Several important error sources are not included in the used model. For example, atmospheric effects, ephemeris errors and satellite clock offset errors are not included in this study. In addition, the environment presented in Section 3 and the propagation of the waves are kept simple. As such, we do not consider internal structures, conductive media, diffraction or transmittance. In this way, we are keeping to analytic insight into the main contributions. As a result, the presented results in Section 4 do not represent the expected ranging errors for LEO-PNT satellites; they should only be compared with other results in this work to understand the multipath behaviour of LEO-PNT systems.

3. Simulation Scenario

This section delineates the details of the specific simulated scenario used to analyse multipath errors in LEO-PNT systems. First, we introduce the geometry and material properties of the scenario. Next, the geometric properties of the different considered reflections are presented. Afterwards, the satellite orbits and signal properties are discussed.

3.1. Multipath Environment

The scenario considered in this study is illustrated in Figure 1. A static receiver is placed at a height h_{rx} at a distance d from a tall building with height h_b . The wall from the building on which the rays will reflect is made of concrete, with a refractive index n_c . We do not consider internal reflections as the attenuation of L-, S- and C-band signals in concrete is high [8], rendering the internal reflections insignificant. The ground is considered dry, with refractive index n_g . The air has a refractive index of n_a . The values used in the simulation [9] can be found in Table 1.

Table 1. The used values of the parameters in the presented scenario.

Parameters	d	h_{rx}	h_b	n_a	n_c	n_g
Value	20 m	2 m	50 m	1	3	4

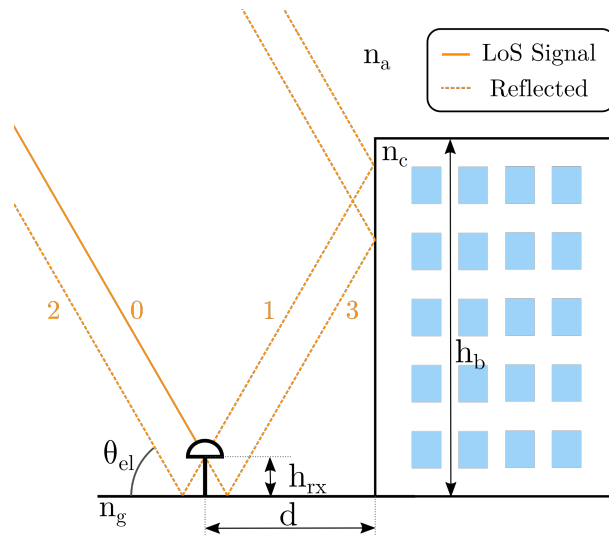


Figure 1. The scenario studied in this paper. A static receiver is placed above the ground next to a high building made of concrete. The satellites rise on the left of the scenario and move overhead. Together with the direct signal, we consider three reflected multipath components.

3.2. Signal Components

In this study, we employ a four-ray model. We consider the direct signal, a ground reflection, a wall reflection and a double reflection using the wall and ground.

To calculate the influence of each of the components, several parameters have to be known. The first parameter is the multipath delay Δt of the reflected signals. The multipath delay is related to the extra distance Δd the reflected signal travels before reaching the receiver. To calculate the delay, the distance must be divided by the propagation speed of the waves, i.e., the speed of light. The next parameter is the elevation cut-off angle θ_c , above which there is no reflection. This cut-off is only present for reflections on the building. In addition, to calculate the reflection coefficients, the incidence angle θ_i has to be determined. And to end, the angle of the incoming wave at the receiver θ_{rx} is needed to calculate the antenna gain. Table 2 lists for each signal component the discussed geometric parameters.

Table 2. Geometric characteristics of the different signal components.

Signal	Direct	Ground	Wall	Wall-Ground
k	0	1	2	3
Δd	0	$2h_{rx} \sin \theta_{el}$	$2d \cos \theta_{el}$	$2h_{rx} \sin \theta_{el} + 2d \cos \theta_{el}$
θ_c	/	/	$\arctan\left(\frac{h_b - h_{rx}}{d}\right)$	$\arctan\left(\frac{h_b + h_{rx}}{d}\right)$
θ_i	/	$90 - \theta_{el}$	θ_{el}	$\theta_{el}, 90 - \theta_{el}$
θ_{rx}	θ_{el}	$-\theta_{el}$	$180 - \theta_{el}$	$180 + \theta_{el}$

To calculate the amplitude of the signal, the RIP of a receiver on Earth needs to be known. Braasch et al. [10] report the RIP of typical MEO GNSSs. There is no public RIP model for LEO-PNT satellites, so we assume the same RIP for both the MEO and LEO systems. In addition, the antenna gain pattern is needed to compute the signal amplitude. The antenna pattern for RHCP and LHCP signals presented by Yang et al. is used [11]. The resulting C/N_0 value for the LoS signal ranges from 40 dB-Hz at the horizon to 57 dB-Hz when the satellites are directly overhead.

The receiving antenna is mainly sensitive to RHCP waves, so the RHCP component of the reflections will be the main influence on the localisation performance of the GNSS receiver. In the presented scenario, at low elevation, the ground reflection is dominant (Figure 2). At higher elevations, the wall reflection becomes the dominant reflection. The

incoming wave from the wall reflection arrives with a positive elevation angle. Therefore, the antenna will not be able to mitigate the RHCP component of this reflected signal.

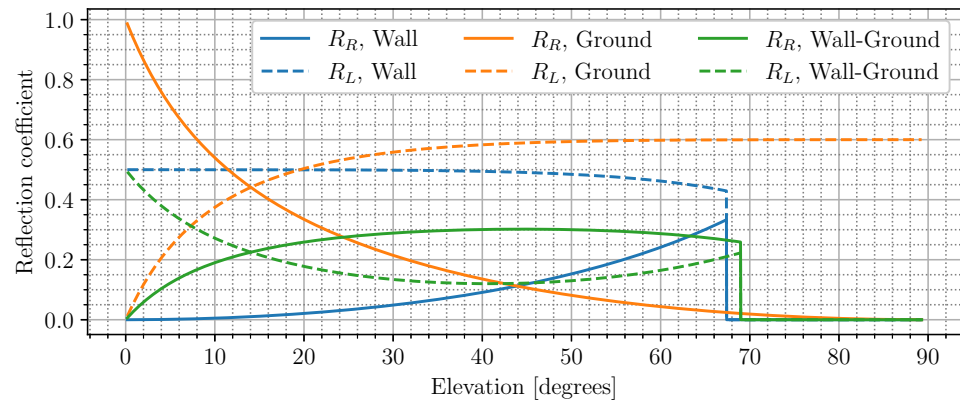


Figure 2. The reflection coefficient R for the different reflected signals and polarisations. Note the cut-off angle of 67 degrees for the wall reflection and 69 degrees for the wall-ground reflection.

3.3. Satellite Orbits

As the focus of this study is on the influence of the height of the satellite orbits, the orbits are simply modelled as perfect circles around the centre of the Earth. We consider four different orbit heights. Three of them are LEO orbits, with a height of 500 km, 1000 km and 1500 km. The fourth orbit is an MEO orbit at a height of 23,222 km, the same height as the Galileo constellation. During the simulation, only a half-pass is simulated, where the satellite rises from the horizon to an elevation of 90 degrees.

3.4. PNT Signals

During the simulation, only the output value of the Early (E), Prompt (P) and Late (L) correlators is computed. The E-L spacing is 1 chip, with P located in the middle of E and L. The correlation peak is based on a GPS L5-like signal with a chipping rate of 10.23 MHz. The receiver has a sampling frequency of 20.46 MHz and a bandwidth of 51.15 MHz.

The values of the E, P and L outputs depend on several factors. The first factor is the code offset between the sampling point and the signal. The second factor is the phase offset between the signal and the estimated phase at the PLL. The third factor is the frequency offset between the estimated frequency and the actual signal. The last factor is the amplitude of the signal component. We do not consider navigation bits.

The E, P and L values are calculated for all different multipath components. Next, they are summed together to create the E, P and L values of the composite signal. Afterwards, noise is added. The correlator outputs are used to calculate the discriminator outputs, which in turn are used by the non-coherent DLL and PLL to update their states.

We consider three carrier frequencies. The first frequency is the GPS L1 frequency. This frequency is the oldest frequency in use by current MEO GNSS systems. We expect that upcoming LEO-PNT systems will transmit a signal in the neighbourhood of the L1 frequency. In addition, new frequency bands are proposed for the upcoming LEO-PNT systems, both in the S- and C-band. Therefore, we also analyse S- and C-band signals at 2491 MHz and 5020 MHz, respectively.

4. Results

This section discusses the results of the presented simulations. To analyse the impact of the multipath error when using LEO satellites, several experiments are designed. We will discuss for each experiment the simulation settings and the corresponding results.

4.1. Influence of the Orbit Height

During the first experiment, the influence of the orbit height of the satellite is analysed. The rate at which the elevation angle varies depends on the orbit height. One pass of an MEO GNSS satellite is in the order of hours, while for an LEO satellite it is in the order of minutes. This large difference in the orbit period translates into a large difference in the change in the elevation angle. The hypothesis is that the multipath error decreases due to the faster change in the phase difference between the LoS signal and the reflected signals.

For this experiment, the orbit height is varied, $h = \{500, 1000, 1500, 23,222\}$ km, while the L-band is used as carrier frequency. The code-range error is shown in Figure 3. The first observation is that the code-range error induced by multipath effects is strongly decreased for LEO satellites in comparison to their MEO counterparts. For low elevations, we observe multipath errors that are equally large for both LEO and MEO satellites. However, when the satellites' elevation rises, a clear difference between the different orbit heights becomes visible. A strong reflection of the signal on the nearby building induces a large error in the MEO scenario. Due to the large incidence angle, a significant RHCP component is still present in the signal after the reflection. At an elevation of 66 degrees, an RMSE value of up to 2.40 m is recorded, while for the LEO satellites, the RMSE is much smaller, from 0.096 m to 0.303 m (Table 3). This is a decrease of up to 96%. Over the full simulation, the RMSE of the code range is reduced by up to 87% by employing LEO satellites.

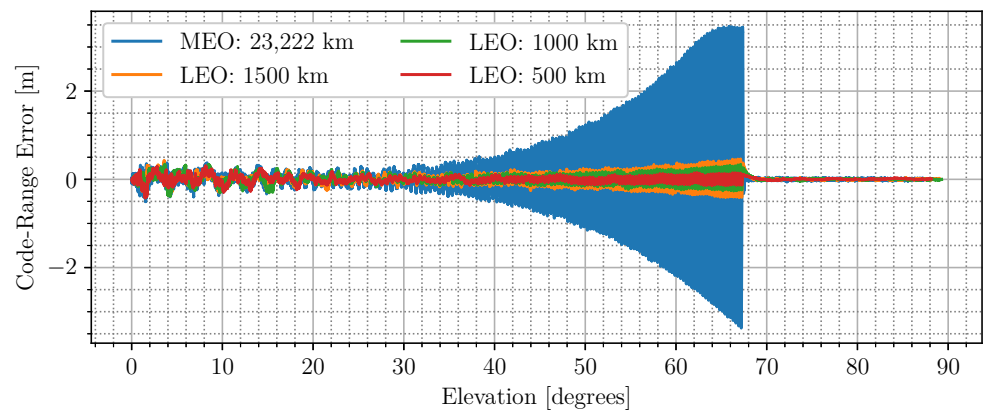


Figure 3. Code-range error versus orbit height, L-band. The strong reflection on the building as the elevation angle of the satellite increases only strongly impacts the MEO system. For LEO systems, the multipath errors are suppressed when the elevation angle increases. Note that above 67 degrees elevation, the wall reflection disappears.

Table 3. Comparing the influence of the orbit height.

Orbit Height	23,222 km	1500 km	1000 km	500 km
Overall RMSE (m)	0.756	0.120	0.111	0.098
Reduction in comparison to MEO	0%	84.1%	85.4%	87.0%
RMSE at $\theta_{el} = 66^\circ$ (m)	2.397	0.303	0.199	0.096
Reduction in comparison to MEO	0%	87.4%	91.7%	96.0%
Max phase delay rate (Hz)	0.042	0.992	1.540	3.155
Increase factor in comparison to MEO	1	23.62	36.67	75.12

This behaviour can be explained when we calculate the phase delay rate. The phase delay is the difference in phase between the LoS component and an indirect multipath component. In this case, we will only study the wall reflection as this has the largest influence in this scenario. The phase delay rate is the derivative of the phase delay over time. It illustrates how fast the phase is rotating the correlation peak of the indirect signal in the complex plane. Figure 4 shows the phase delay rate for the wall reflection as a

function of the elevation angle. For LEO systems, the phase delay rate reaches frequencies higher than the bandwidth (BW) of the DLL, which was set to 0.25 Hz for this study. Our simulations show that the maximum phase delay rate is increased up to 75 times by employing LEO satellites (Table 3). As a result, the DLL starts treating the multipath components as noise and filters out their influence. This behaviour is only present above a certain elevation angle, which depends on the orbit height of the satellite.

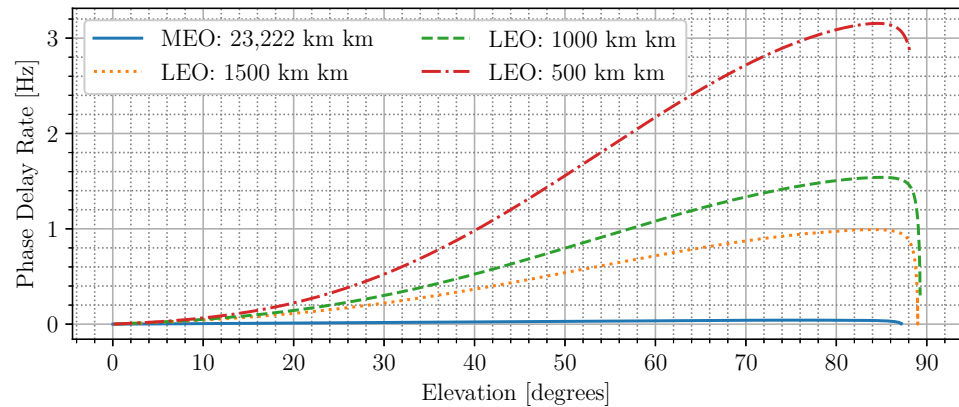


Figure 4. Phase delay rate of the wall reflection for the different orbit heights. Due to the faster geometry change of lower orbits, the phase delay rate becomes larger. This effect is increased for high elevations as LEO satellites have higher perceived mobility at high elevations for ground users.

4.2. Influence of the DLL Bandwidth

In the second experiment, we investigate the influence of the DLL BW on the code-range error. Three different values of the DLL BW are evaluated: $DLL_{BW} = \{1, 0.25, 0.05\}$ Hz. The satellite orbits at a height of 1000 km using an L-band signal. The code-range error is shown in Figure 5. At low elevations, the amplitude of the error is only slightly decreased by decreasing the DLL BW; however, at higher elevations, the error amplitude is strongly reduced as the filtering effect has become larger.

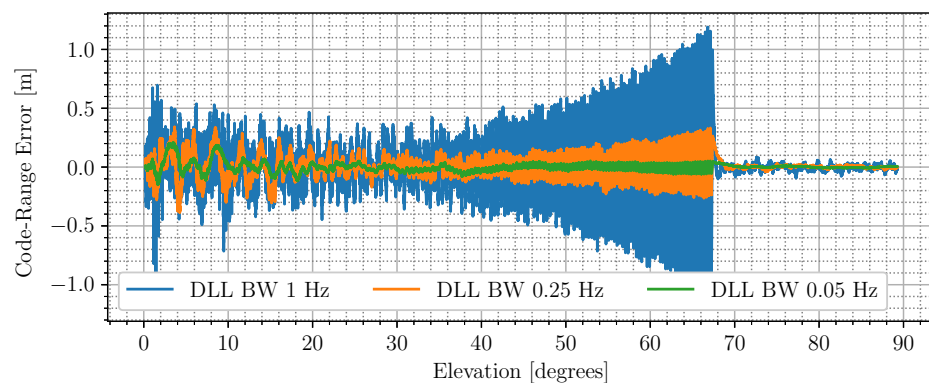


Figure 5. Code-range error versus DLL bandwidth. The considered satellite orbits are at a height of 1000 km. When lowering the DLL bandwidth, the code range error decreases and vice versa.

4.3. Influence of Carrier Frequency

As the reported effect is coupled to the phase delay, the wavelength of the carrier has an influence as well. To illustrate this effect, the scenario was simulated using an orbit height of 1000 km while using three different carrier frequencies: L1 (1575.42 MHz), S-band (2491 MHz) and C-band (5020 MHz). For this simulation, we assume that the material properties are equal for the considered frequencies. At elevations below 30 degrees, no significant difference is noticeable; above this elevation, the S- and C-band signals have a

decreased ranging error (Figure 6). In comparison to the L-band, the ranging error decreases by 10.8% for the S-band and 24.3% for the C-band (Table 4).

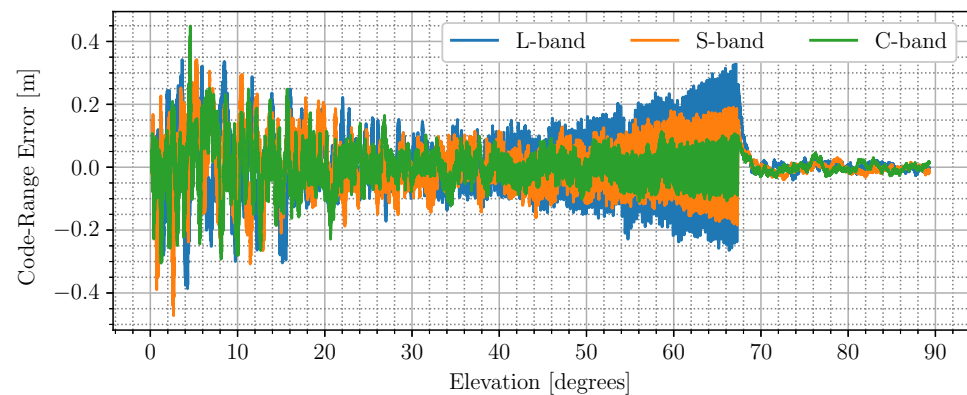


Figure 6. As the reported effect is coupled to the wavelength of the carrier frequency, the multipath error decreases with increasing frequency.

Table 4. Root mean squared error of the code-range error as a function of the frequency band.

Frequency	L-Band	S-Band	C-Band
Overall RMSE (m)	0.111	0.099	0.084
Reduction in comparison to L-band	0%	10.8%	24.3%
RMSE at $\theta_{el} = 66^\circ$ (m)	0.199	0.123	0.064
Reduction in comparison to L-band	0%	38.2%	67.8%
Reduction in wavelength λ	0%	36.8%	68.6%

5. Conclusions

Multipath-induced code-range errors are strongly reduced in LEO-PNT systems for fast-changing multipath components. Our simulations show an overall reduction in the code-range error of 87% when comparing an MEO satellite to an LEO satellite at a height of 500 km. We attribute this reduction to the phase delay rate, which rises above the DLL BW for fast-changing multipath components. The phase delay rate is up to 75 times larger for LEO than for MEO signals. As a result, the DLL BW has a large influence on the experienced multipath code error in LEO-PNT systems. In addition, including higher carrier frequencies in LEO-PNT can further reduce multipath code-range errors. In comparison to L-band signals, our simulations show a decrease of 10.8% for S-band signals and 24.3% for C-band signals.

Author Contributions: Conceptualization, S.D.B., J.-M.S. and W.D.W.; methodology, S.D.B. and W.D.W.; software, S.D.B.; validation, J.-M.S. and W.D.W.; formal analysis, S.D.B.; investigation, S.D.B.; resources, J.-M.S.; data curation, S.D.B.; writing—original draft preparation, S.D.B.; writing—review and editing, S.D.B.; visualization, S.D.B.; supervision, W.D.W.; project administration, W.D.W.; funding acquisition, S.D.B. and W.D.W. All authors have read and agreed to the published version of the manuscript.

Funding: This research was partially funded by VLAIO, grant number: HBC.2022.0169.

Institutional Review Board Statement: Not applicable.

Informed Consent Statement: Not applicable.

Data Availability Statement: The data presented in this study are available on request from the corresponding author. The data are not publicly available due to strict IP management.

Conflicts of Interest: Septentrio is a GNSS receiver manufacturer. As such research into novel GNSS opportunities and GNSS receiver technology is of high interest to the company.

References

1. Li, X.; Ma, F.; Li, X.; Lv, H.; Bian, L.; Jiang, Z.; Zhang, X. LEO constellation-augmented multi-GNSS for rapid PPP convergence. *J. Geod.* **2019**, *93*, 749–764. [[CrossRef](#)]
2. Reid, T.; Banville, S.; Chan, B.; Gunning, K.; Manning, B.; Marathe, T.; Neish, A.; Perkins, A.; Sibois, A. PULSAR: A New Generation of Commercial Satellite Navigation. In Proceedings of the ION GNSS+ 2022, Denver, CO, USA, 19–23 September 2022.
3. Yuan, J.; Zhou, S.; Hu, X.; Yang, L.; Cao, J.; Li, K.; Liao, M. Impact of Attitude Model, Phase Wind-Up and Phase Center Variation on Precise Orbit and Clock Offset Determination of GRACE-FO and CentiSpace-1. *Remote Sens.* **2021**, *13*, 2636. [[CrossRef](#)]
4. Lawrence, D.; Cobb, H.S.; Gutt, G.; O'Connor, M.; Reid, T.G.; Walter, T. Navigation from LEO, GPS World, July 2017. Available online: https://web.stanford.edu/group/scpnt/gpslab/pubs/papers/Lawrence_GPSWorld_July2017.pdf (accessed on 27 November 2023).
5. Iannucci, P.A.; Humphreys, T.E. Economical Fused LEO GNSS. In Proceedings of the 2020 IEEE/ION Position, Location and Navigation Symposium (PLANS), Portland, OR, USA, 20–23 April 2020; pp. 426–443. [[CrossRef](#)]
6. Peatross, J.; Ware, M. Physics of Light and Optics. 2015. Available online: <https://optics.byu.edu/> (accessed on 8 March 2023).
7. Smyrniaios, M.; Schön, S.; Nicolás, M.L. Multipath Propagation, Characterization and Modeling in GNSS. In *Geodetic Sciences*; Jin, S., Ed.; IntechOpen: Rijeka, Croatia, 2013; Chapter 2. [[CrossRef](#)]
8. Stone, W. *Electromagnetic Signal Attenuation in Construction Materials*; NIST: Gaithersburg, MD, USA, 1997. [[CrossRef](#)]
9. Hannah, B.M. Modelling and Simulation of GPS Multipath Propagation. Ph.D. Thesis, Queensland University of Technology, Brisbane, QLD, Australia, 2001.
10. Braasch, M.; Dempster, A. Tutorial: GPS receiver architectures, front-end and baseband signal processing. *IEEE Aerosp. Electron. Syst. Mag.* **2019**, *34*, 20–37. [[CrossRef](#)]
11. Yang, N.; Freestone, J. High-performance GNSS antennas with phase-reversal quadrature feeding network and parasitic circular array. In Proceedings of the 29th International Technical Meeting of the Satellite Division of The Institute of Navigation (ION GNSS+ 2016), Portland, OR, USA, 12–16 September 2016; pp. 364–372.

Disclaimer/Publisher's Note: The statements, opinions and data contained in all publications are solely those of the individual author(s) and contributor(s) and not of MDPI and/or the editor(s). MDPI and/or the editor(s) disclaim responsibility for any injury to people or property resulting from any ideas, methods, instructions or products referred to in the content.